Nano Research
2024, 17(5): 4069–4078

ISSN 1998-0124 CN 11-5974/O4
https://doi.org/10.1007/s12274-023-6298-2

Research Article

An effective strategy for dendrite free Li metal anodes: Nickel foam decorated with high lattice-matching CoN and CoF_2 nanosheets for dense deposition

Wenlong Liu[1], Jianzong Man[2], Xiaodong Sun[1], Ning Zhang[1], Yehong Du[3], Kun Liu[1], Zhongsheng Wen[1], Song Li[1], and Juncai Sun[1] (✉)

[1] *Institute of Materials and Technology, Dalian Maritime University, Dalian 116026, China*
[2] *Shandong Provinvial Key Laboratory of Chemical Energy Storage and Novel Cell Technology, and School of Chemistry and Chemical enginnering, Liaocheng University, Liaocheng 252000, China*
[3] *Department of Public Security Management, Liaoning Police College, Dalian 116036, China*

Received: 11 September 2023 / **Revised:** 24 October 2023 / **Accepted:** 30 October 2023

ABSTRACT

The notorious dendrite and infinite volume change seriously restrict the advancement of lithium metal anodes (LMAs), during the long-term process of stripping/plating. Herein, the nanosheets of metal fluoride (CoF_2) and metal nitride (CoN) with magnificent lithiophilicity on the nickel (Ni) foam are designed as the "regulator" to uniform the Li plating and build stronger solid electrolyte interface (SEI) layer for dendrite free LMAs. The Ni foam offers abundant space to receive deposited Li metal. The CoN nanosheets can guarantee the fast transfer of electrons, which provides a stable interface of Li^+ reduction. Moreover, the nanosheet structure with lithiophilicity would accelerate the move of Li^+ and decrease the nucleation barrier, due to the high lattice-matching of Li and CoN. Meanwhile, the CoF_2 could increase the content of F (LiF) in the SEI layer, which enhances the strength and avoids the destruction of SEI layer. With the cooperation of CoN and CoF_2, the composited anode (Li/NF@CNCF) exhibits ultra-long cycle performance (more than 1200 h) and fantastic structure stability at 1 $mA \cdot cm^{-2}$ with 1 $mAh \cdot cm^{-2}$. Based on the $LiFePO_4$ and Li/NF@CNCF, the full cells deliver excellent specifical capacity and steady coulombic efficiency. The strategy contributes an effective approach to alleviate the issues of lithium metal anodes in the field of LMAs.

KEYWORDS

CoN and CoF_2, lattice-matching, nanosheet, lithiophilicity, lithium metal anodes

1 Introduction

Lithium (Li) ion battery has attracted much interest with excellent and stable electrochemical performance, but the traditional anode material (graphite) cannot meet the demands of people. According to the characteristic advantages, such as the highest specific capacity (3860 $mAh \cdot g^{-1}$) [1], low potential voltage (−3.04 V vs. standard hydrogen electrode) [2], and high energy density, Li metal anodes (LMAs) would like to be the ideal anode materials [3–5]. The energy storage of LMAs depends on the stripping/plating of Li^+ on the anodes.

However, the growth of deposited Li usually cannot keep densification and uniformity. The uneven deposition of Li^+ would lead to the Li dendrite [6, 7], and the "tip effect" [8–10] intensifies the electric field to attract the Li^+ at around and assists the growth of dendritic Li. The uncontrollable and continuous dendrite would puncture the solid electrolyte interface (SEI) layer and separator to fail the battery [11]. Meanwhile, the SEI layer, which appears at the surface of LMAs, is formed by the reaction of Li metal and electrolyte [12–15]. The fresh Li can be protected by the SEI layer, even though consumes the Li^+ of the battery system. Nevertheless, the infinite volume change could destroy the integrity of SEI layer, and the fresh Li contacts with electrolyte by the crack. The dendritic Li and rebuilding of SEI layer are the main sources of capacity and coulombic efficiency (CE) decline [16–19].

The above two issues (dendritic Li and volume change) restrict the application of LMAs, and many strategies, such as interlayer between LMAs and electrolyte [20], appropriate additive of electrolyte [21], rational design of framework (collector) [22], and artificial SEI layer [12], etc, have been approved to restrain the disadvantages. Nickel (Ni) foam as the collector receives attention from researchers (relies on the rich reserves and low cost), which is usually used as the filler material of cells. However, the low lithiophilicity of Ni foam would increase the nucleation barrier and make the inhomogeneous Li^+ deposition. Modification with lithiophilic materials is an effective way to reduce the nucleation barrier. Classical lithiophilic materials include metallic oxide [23], metallic nitride [24], metallic halide [25], functional groups [26], and defects [27], etc. Metallic nitride exhibits exclusive superiority, because of its high conductivity and stability. Man et al. [28] have designed lithiophilic honeycomb-like Ni_3N nanosheet to modify Ni foam. The surface of Ni foam is divided into many micro-regions and regular deposition of Li^+. Tang et al. [29] prepared business copper decorated *in situ* with Cu_3N nanowires, which can decrease the real current density, relax the volume change, and

Address correspondence to sunjc@dlmu.edu.cn

increase the dynamics of Li^+ transfer in the SEI layer. It is worth mentioning that the composition of SEI layer (such as the Li_3N phase in SEI layer) is not only impacted by the electrolyte, but also the electrode [30]. In addition, the lattice coordination with Li of most metallic nitrides is poor, which leads to the large difficulty between the Li and substrate (obstruction of Li deposition) [31]. So, the selection of suitable lithiophilic material to decorate Ni foam plays an important role for excellent LMAs.

Herein, the nanosheets of metal fluoride (CoF_2) and metal nitride (CoN) with magnificent lithiophilicity on the Ni foam (NF@CNCF) are designed as the "regulator" by hydrothermal method and post-calcination. Benefiting from the rich interspace, abundant nucleation sites, and buffer space, the behavior of Li^+ stripping/plating is upgraded by the Ni foam. The CNCF nanosheet structure provides a fast way for Li^+ transfer, which improves the dynamic performance. And, the existence of CoN sensibly improves the lithiophilicity of Ni foam and decreases the nucleation barrier of Li^+, owing to the higher lattice coordination, compared with other metallic nitrides. Meanwhile, the high conductivity of CoN promises a stable interface of Li^+ reaction. Besides, the CoF_2 of CNCF could increase the content of F, which means more LiF in the SEI layer and high strength of the SEI layer for stable LMAs. Profited from the cooperation of the NF and CNCF, the cyclability and stability of LMAs are developed, obviously. With 1 $mA{\cdot}cm^{-2}$ at 1 $mAh{\cdot}cm^{-2}$, the symmetric cells with NF@CNCF show outstanding electrochemical performance (polarization voltage keeps at 9 mV more than 1200 h) and stable CE (settle around 98% more than 600 cycles). The full cells with NF@CNCF and $LiFePO_4$ deliver excellent performance (the specifical capacity keeps at 121.2 $mAh{\cdot}g^{-1}$ after 200 cycles under 1 C), indicating that the NF@CNCF has the potential to apply in business.

2 Experimental section

2.1 The pretreatment of Ni foam

The Ni foam in this paper was purchased from Foammetal New Material Co. Ltd. Before the decoration, the Ni foam was individually ultra-sonic cleaned in deionized water, ethanol, and acetone for 15 min to remove the impurity. Then, the cleaned Ni foam was dried for 12 h at 80 °C.

2.2 The preparation of NF@$CoF_{1.3}(OH)_{0.7}$

0.58 g $Co(NO_3)_2{\cdot}6H_2O$, 0.3 g NH_4F, and 0.96 g urea were added to 30 mL deionized water, and stirred for 30 min. Then, the Ni foam was cut into circular electrodes and the diameter was 10 mm. After that, the mixed solution and the Ni foam electrodes were removed into the sealed Teflon-lined autoclave and kept at 120 °C for 8 h. Then, the Ni foam after hydrothermal was ultra-sonic cleaned for 15 min in deionized water and ethanol, separately. After that, the Ni foam was dried at 80 °C for 12 h.

2.3 The preparation of the NF@CNCF

The dry NF@ $CoF_{1.3}(OH)_{0.7}$ was calcined in Ar_2 at 450 °C for 2 h with the tube furnace, and the heating rate was 2 $°C{\cdot}min^{-1}$.

2.4 Characterization

The X-ray diffraction (XRD) was chosen to analyze the crystal structure at room temperature by using the Rigaku-D/MAX-3A with Cu-Kα radiation, and the λ_{Cu} was 0.154 nm. And, the surface morphology and elements distribution of samples were observed by field-emission scanning electron microscopy (FE-SEM, SUPRA 55 SAPPHIRE with energy dispersive X-ray detector) and energy dispersive spectrometer (EDS). The high-resolution images and the diffraction spots were observed by the transmission electron microscopy (TEM, FEI Tecnai F20) The valence state and bond energy were identified via X-ray photoelectron spectroscopy (XPS) with K-Alpha 1063, and the standard peak of C 1s (284.6 eV) was proofread.

In this paper, all of the batteries were packed in the glove box (MBRAUN UNllab Plus) filled with Ar_2 and the component of O_2 and H_2 below 0.01 ppm. Herein, 1.0 mol LiTFSI (Li difluoromethane sulfimide) was used as the electrolyte, 4.0% $LiNO_3$ was added into 1,3-dioxane (DOL) and 1,2-dimethoxyethane (DME) (v:v = 1:1). The type of battery was CR2025, and the stuffing was Ni foam. The LMAs of NF@CNCF (Li/NF@CNCF) and NF (Li/NF) were prepared by platting 5 $mAh{\cdot}cm^{-2}$ Li on the pure electrodes at 1 $mA{\cdot}cm^{-2}$, separately. The symmetric cells of NF@CNCF and NF were assembled with two Li/NF@CNCF and Li/NF as electrodes. The Li||NF@CNCF and Li||NF were packed to test the CE of the samples. And, the full cells of CNCF and NF were fabricated with $LiFePO_4$ (LFP) matching to Li/NF@CNCF and Li/NF, individually. In the system of full cells, acetylene, LFP, and carboxymethyl cellulose (CMC) were added to deionized water with the ratio of 2:7:1 to compose the slurry, and then, coated on the Al foil. Afterward, the electrode of LFP was dried in the vacuum oven at 80 °C for 12 h. The electrochemical performance was tested with the LAND battery system (CT2001A), and the electrochemical impedance spectroscopy (EIS) was carried out on the electrochemical workstation (Chenhua Chi 600) with a frequency range of 0.01 Hz–100 kHz.

3 Results and discussion

The NF is the excellent bulk of LMAs, the abundant interspace relaxes the volume change of electrodes. Figure S1 in the Electronic Supplementary Material (ESM) is the preparation flowchart of NF@CNCF. In the process of hydrothermal reaction, nanosheets of $CoF_{1.3}(OH)_{0.7}$ were successfully produced, and some amorphous carbon was generated from urea. Herein, the amorphous carbon is bonded with the N elements. Meanwhile, the NF not only acts as the framework, but also works as the catalyzer. During the calcination process, CoN and CoF_2 are generated, because the amorphous carbon is oxidized to CO_2 by the reaction with hydroxyl and outed. And, the Co is reacted with F and N to form CoN and CoF_2. Compared with other methods, the calcination way is facile and novel based on the flaky and fluorinated hydroxide, which provides a novel approach to obtain the metal nitride.

Besides, the NF provides enough space for deposited Li metal at the macro scale, the nanosheets of CoN and CoF_2 (CNCF) regulate the local distribution of Li^+. The lattice spacing of Li ((110), 0.248 nm, JCPDS card #15-0401) can superbly match with CoN (111), so the high lattice coordination of CoN and Li facilitates the high lithiophilicity of CNCF, effectively. According to the density functional theory (DFT), the interfacial energy of Li (110) and CoN (111) is −1.184 $J{\cdot}m^{-2}$ [24], which indicates the CoN nanosheets have good lithiophilicity. Figure 1 shows the diagrammatic sketch of Li^+ deposition on the different collectors. At the initial stage of deposition on NF, the arrangement of Li^+ is uneven and aggregative, due to the poor lithiophilicity. With the increase of deposition, the Li^+ prefers to gather in the protrusion, own to the short transportation and strong electric field. The inhomogeneous deposition would lead to the growth of dendrites. On the contrary, the lihtiophilic CNCF attracts Li^+ to deposit on nanosheets, which causes the uniform growth of deposited Li^+. So, the local deposition is regulated by the CNCF, and generates the dense and smooth deposited Li layer.

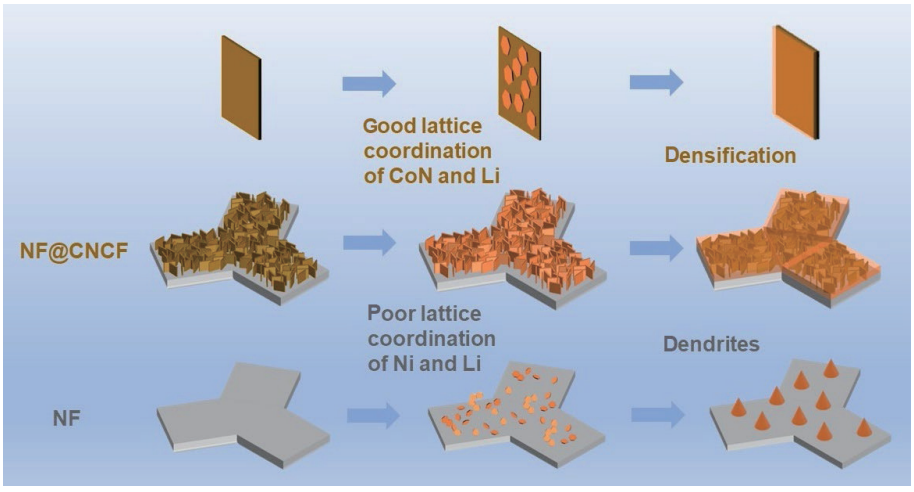

Figure 1 The diagrammatic sketch of Li^+ deposition on the NF and NF@CNCF, separately.

The crystal structure of samples was characterized by the XRD, and the range of the incident angle is from 10° to 90°. Figure S2(a) in the ESM shows the XRD patterns of NF, NF@$CoF_{1.3}(OH)_{0.7}$, and NF@CNCF, respectively. Some weak differences appear in the different samples, due to the too strong background of Ni foam. To clearly analysis the phase structure, the pure Ni foam, $CoF_{1.3}(OH)_{0.7}$, and CNCF were prepared and characterized at the same conditions. Figure S2(b) in the ESM is the XRD of Ni foam, three peaks (44.5°, 51.8°, and 76.4°) occur and match with the crystal plane of (111), (200), and (220) (PDF#04-0850). The peaks of $CoF_{1.3}(OH)_{0.7}$ (Fig. S2(c) in the ESM) can wonderfully correspond to the stranded card (PDF#18-0405). In the XRD pattern of CNCF (Fig. S2(d) in the ESM), two different crystal structures (CoN and CoF_2) can be split, which proves the representation of CoN and CoF_2 (PDF#33-0417 and PDF#16-0116). Based on the Bragg equation to calculate the lattice spacing

$$2d\sin\theta = \lambda \quad (1)$$

Herein, the d represents lattice spacing, the θ represents the incidence angle, and the λ is the wavelength. Therefore, the peak at 36.2° can match with the (111) plane of CoN and the lattice spacing is about 0.248 nm, which further ensures the lattice match of CNCF and Li. Compared with all the spectrograms, the CNCF can be proven to grow on the NF.

The micromorphology and element distribution were observed with the SEM and EDS, separately. Figure S3 in the ESM is the SEM images of NF at different magnifications, the surface of pure NF is smooth and flat. The pure $CoF_{1.3}(OH)_{0.7}$ and CNCF images are shown in Figs. S4(a)–S4(d) in the ESM. After the hydrothermal reaction, $CoF_{1.3}(OH)_{0.7}$ nanoneedles grow on the surface of the NF. The local nanoneedles are arranged into arrays (Fig. 2(a)), which uniformly grow on the bulk (Figs. 2(b) and 2(c)). With the calcination, the arrays of $CoF_{1.3}(OH)_{0.7}$ turn into the nanosheets of CoN and CoF_2 (Figs. 2(d)–2(f)). With the EDS (Figs. S5(a) and S5(b) in the ESM), the elemental distribution of simples is homogeneous. The detailed structural analysis of CNCF was carried out by the TEM. Figure 2(g) is the high-resolution TEM image of CNCF, and the diffraction rings and lattice fringe are shown in Figs. 2(h) and 2(i). According to the calculation of the diameter, the four diffractions can be matched with the crystal plane (311) of CoN and the (002), (111), and (110) of CoF_2. In the local of CNCF, three different spacings of the lattice fringe (0.248, 0.214, and 0.175 nm) appear and can be mated of the (220), (200) of CoN and (211) of CoF_2. Combined with the result of XRD, the lattice structure of CNCF would be characterized, and the existence of CoN and CoF_2 is further proved.

The chemical composition of the CNCF was characterized by the XPS, and the peaks fitting of valence state and bonding were completed by Thermo Advantage. Before the fitting, the standard peak of C 1s (284.6 eV) was corrected. Figure S6 in the ESM is the full XPS spectra of CNCF, the C, Co, N, and F peaks appear on it, separately. In the high-resolution spectra of C 1s (Fig. 3(a)), there are three peaks and the background is from 281.58 to 292.38 eV. The peaks at 284.6, 286.48, and 288.98 eV can be matched with the bonds of C–C, C–O/C–N, and C–F, individually [32]. According to the calculation, the equivalent homogeneous composition of the above bonds is 62.7%, 10.97%, and 26.33%, respectively. Figure 3(b) shows the high-resolution spectra of Co 2p, and the background is from 775.98 to 809.28 eV. The peaks at 780.84 and 796.96 eV are regarded as the Co^{3+}; 783.47 and L 800.05 eV are regarded as the Co^{2+}; and the 786.75 and 802.98 eV are the satellites of Co [33]. With the calculation, the equivalent homogeneous composition of Co^{3+} and Co^{2+} is 53.2% and 20.6%, separately. Figure 3(c) is the high-resolution spectra of F 1s, and the background of F is from 679.48 to 690.88 eV [34]. The peak at 684.01 eV is regarded as the F–Co. In the high-resolution of N (Fig. 3(d)), the background is from 394.88 to 406.78 eV. Meanwhile, the three peaks (397.64, 399.33, and 400.78 eV) can be corresponded to the pyridinic N, N–Co, and pyrrolic N, respectively [33]. With the characterization of XPS, the co-existence of CoN and CoF_2 can be further proved.

The nucleation overpotential (η) is an important parameter to measure the difficulty of Li^+ deposition on the separator. The η is defined as the potential difference between the lowest and stable deposited potential [35]. Figure S7 in the ESM illustrates the η of NF and CNCF at different current densities. At the 1 mA·cm^{-2} (Fig. S7(a) in the ESM), the η_{NF} is about 57.0 mV with the capacity of 5 mAh·cm^{-2}, and the CNCF is just 21.4 mV. The low η of NF@CNCF represents the low nucleation barrier and high lithiophilicity, which can be attributed to the high lattice matching of CoN and Li. When the current density is 3 (Fig. S7(b) in the ESM) and 5 mA·cm^{-2} (Fig. S7(c) in the ESM), the η of CNCF (51.7 mV at 3 mA·cm^{-2} and 136.7 mV at 5 mA·cm^{-2}) is also lower than NF (132.1 mV at 3 mA·cm^{-2} and 212.8 mV at 5 mA·cm^{-2}), respectively. According to Fig. S7(d) in the ESM, the CNCF not only works at low current density, but also shows fantastic electrochemical performance at high current density.

To evaluate the process of Li^+ deposition on the NF and NF@CNCF, the SEM was used to observe the morphology of samples with different sedimentary at various current densities. Under 1 mA·cm^{-2}, the surface of NF (Fig. 4(a)) is smoother than the NF@CNCF (Fig. 4(d)) with 0.5 mAh·cm^{-2} deposited Li, because the sedimentation is too low to cover the layer of

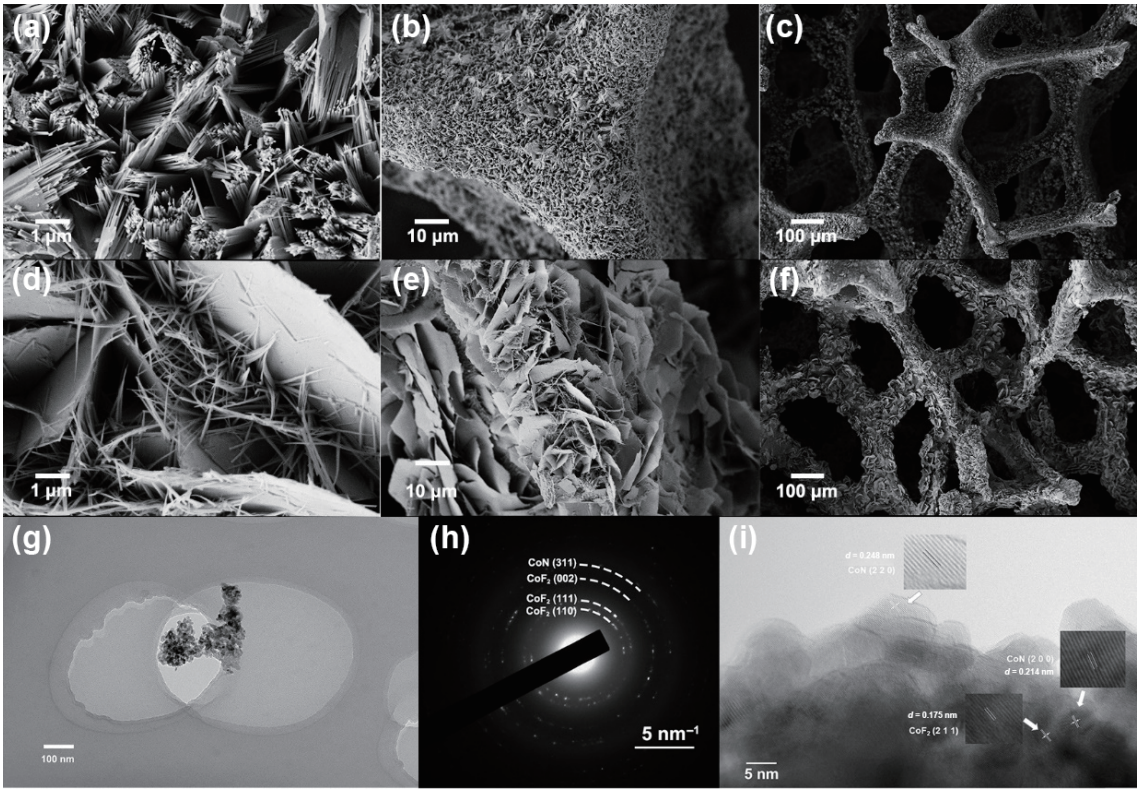

Figure 2 (a)–(c) The SEM images of NF@$CoF_{1.3}(OH)_{0.7}$ at various magnifications. (d)–(f) The SEM images of NF@CNCF at same magnification. (g) The TEM image of CNCF. (h) The diffraction rings of CNCF. (i) The high-resolution TEM of CNCF.

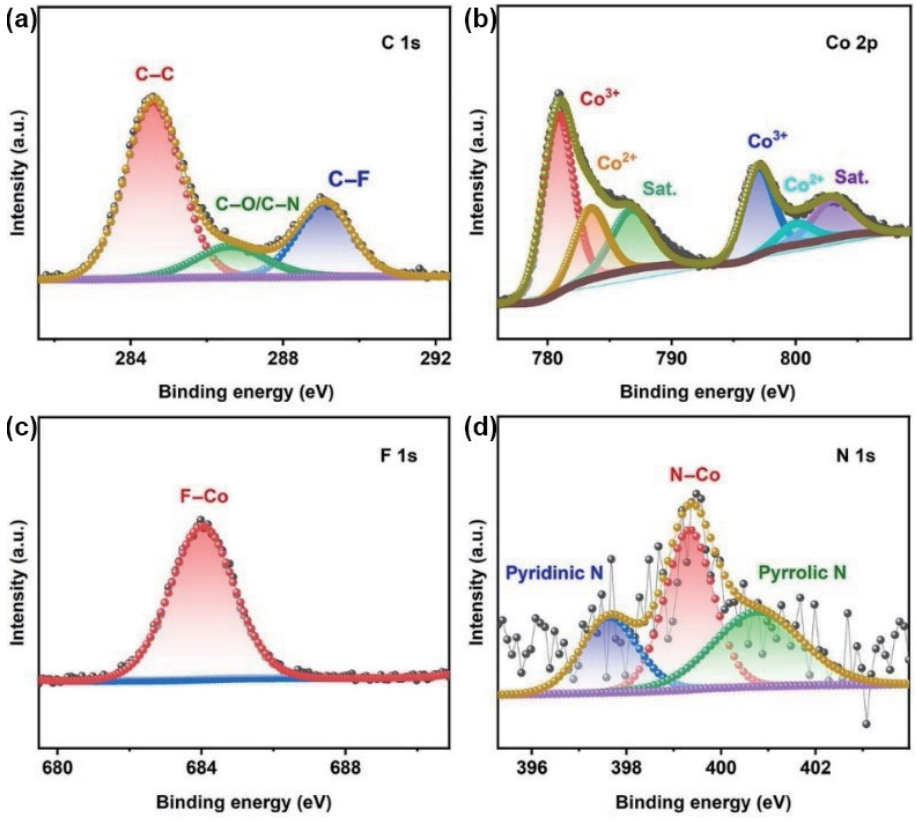

Figure 3 The high-resolution XPS spectra of (a) C, (b) Co, (c) F, and (d) N, respectively.

NF@CNCF nanosheets. With the increasing deposition (1 mAh·cm^{-2}, Fig. 4(b)), some granular protrusions appear on the surface of NF, which is due to uneven deposition by the low lithiophilicity of NF. With 2 mAh·cm^{-2} (Fig. 4(c)), a major of bulges generate on the NF and the deposited morphology has seriously deteriorated. Compared to NF, the surface of NF@CNCF becomes more stable from 0.5 (Fig. 4(d)) to 1 mAh·cm^{-2} (Fig. 4(e)), which can be owned to the high lithiophilicity of CoN and the rich gap as the fast way for Li^+ transfer. So, the deposited Li would be filled in the middle of nanosheets, and the volume change is additionally mitigated. When the deposition is 2 mAh·cm^{-2} (Fig. 4(f)), the Li is still compactly plated on the surface of NF@CNCF. As we all know, the deposited morphology would be more irregular with the rise of current density. At

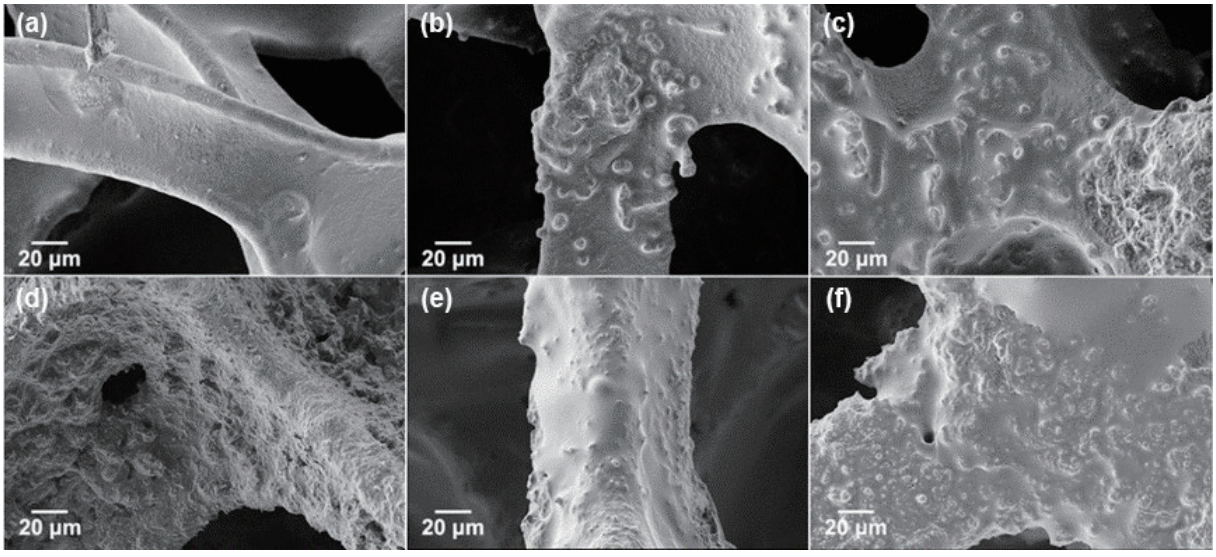

Figure 4 (a)–(c) Under 1 mA·cm^{-2}, the SEM images of NF with 0.5, 1, and 2 mAh·cm^{-2} deposited Li. (d)–(f) The SEM images of CNCF at same condition.

3 mA·cm^{-2} (Fig. S8(a) in the ESM), some pie-deposited Li grows on the NF with 0.5 mAh·cm^{-2}, which means the Li$^+$ prefers to gather in the tip of protruded Li. Figure S8(b) in the ESM shows the SEM image of NF with 1 mAh·cm^{-2} Li, the deposited Li accumulates in the interspace of NF. And, the connection of deposited Li and bulk is weak, which easily breaks away from NF and generates poor activity Li (dead Li). With 2 mAh·cm^{-2} (Fig. S8(c) in the ESM), the deposited Li is loose and the function of NF (relieving the volume change) is greatly impaired. Benefited by the high lithiophilicity and suitable structure design, the deposited behavior of Li$^+$ on NF@CNCF is stable, uniform, and dense. No significant raised Li appears on the NF@CNCF with the deposition of 0.5 (Fig. S8(d) in the ESM), 1 (Fig. S8(e) in the ESM), and 2 mAh·cm^{-2} (Fig. S8(f) in the ESM), separately.

As shown in Fig. S9 in the ESM, the LMAs of NF@CNCF were successfully fabricated by the Li molten-infusion process, and the heating temperature was 240 °C. The electrodes of NF@CNCF and NF were heated over the Li foil in the cases (Figs. S9(a) and S9(d) in the ESM). The brown electrode of NF@CNCF attracts the molten Li to cover the surface slowly when the electrode touches the molten Li. With 5 min (Fig. S9(b) in the ESM), part of the NF@CNCF has turned silver. After 10 min (Fig. S9(c) in the ESM), the surface of the NF@CNCF is completely covered by the molten Li, and the electrodes turn into a bright silver as a whole. The successful preparation indicates that the NF@CNCF possesses high wettability with molten Li. However, the NF electrode cannot recombine with molten Li (Figs. S9(e) and S9(f) in the ESM), even after 20 min, which proves that the porous structure of the NF@CNCF is not the key to improve the wettability with Li. Therefore, the decoration with CNCF plays an important role in good affinity, which can be owned to the high matching lattice between CoN and Li metal [36]. Because the molten Li cannot be flooded into the NF, the cells in this paper choose electroplating as the way to prepare the LMAs.

To test the long-cycle performance of NF@CNCF, the symmetric cells of NF and NF@CNCF were assembled and deposited 5 mAh·cm^{-2} Li at 1 mA·cm^{-2} before the cycles. At 1 mA·cm^{-2} with 1 mAh·cm^{-2} (Fig. 5(a)), the cells of NF can stably operate before 600 h, and the voltage platform keeps about 10 mV. When the cycle exceeds 640 h, the voltage platform rapidly rises and the batteries are damaged, which can be attributed to the destruction of the structure, growth of Li dendrite, and accumulation of "dead Li". When the condition is 3 mA·cm^{-2} and 1 mAh·cm^{-2} (Fig. 5(b)), the cycle life is shorter and the overvoltage is higher (about 60 mV after 80 h). Apparently, the high current density would facilitate the failure of cells. At 5 mA·cm^{-2} (Fig. 5(c)), the cells stably run no more than 60 h, and the overvoltage rapidly rises and fails. Although the porous structure of NF relaxes the volume exchange, the low affinity with Li is a fatal disadvantage for LMAs. Contrast to the NF, the NF@CNCF obtains outstanding cycle performance with the decoration of CoN and CoF_2 nanosheets. As shown in Fig. 5(a), the symmetric cells with CN@CNCF exhibit ultra-long cycle life (more than 1200 h) and lower voltage platform (about 9 mV) than NF at 1 mA·cm^{-2} with 1 mAh·cm^{-2}. Even if the current density increases to 3 and 5 mA·cm^{-2}, the cycle performance of NF@CNCF (run about 33 mV more than 250 h under 3 mA·cm^{-2}, run at 53 mV more than 100 h under 5 mA·cm^{-2}) is better than NF, evidently. As a consequence, the CNCF can effectively improve the cycle stability, lower the overvoltage, and upgrade the electrochemical performance. Meanwhile, the rate performance of samples was tested at different current densities. According to Fig. S10 in the ESM, the voltage platform of NF@CNCF is lower than NF at 1, 2, 3, 5, and 1 mA·cm^{-2}, respectively. And the overvoltage can be restored to the initial cycles after the high current density, which means the NF@CNCF has good structural stability. In addition, the above literature is listed to evaluate this work. Table S1 in the ESM illustrates the overpotential and cycle life of the other paper about Ni foam used in Li metal anodes. Our work has a longer cycle life and lower overpotential at 1 mA·cm^{-2} with 1 mAh·cm^{-2}.

For evaluating the deposited behavior in cycling, SEM is an important way to observe the morphology of LMAs. After 40 cycles (Fig. 6(a)), some mossy Li appears on the surface of NF. With the high magnification (Fig. 6(b)), particle Li distributes on the NF, the coarse and uneven surface would lead to the deterioration of Li sedimentary. As expected, the Li/NF after 100 cycles (Fig. 6(c)) becomes looser than 40 cycles and there are many cracks and holes on the sedimentary under the high magnification (Fig. 6(d)). The porous and loose structure of deposited Li would expand the volume and easily disengage from the Li bulk, which would decrease the CE and electrochemical performance of LMAs. On the contrary, the Li sedimentary is evenly covered on the surface of NF@CNCF (Fig. 6(e)) after 40 cycles. With high magnification (Fig. 6(f)), the surface of NF@CNCF is smoother than NF. After more cycles (100 cycles), the morphology of NF@CNCF (Fig. 6(g)) is similar to 40 cycles. Under high magnification, the surface of NF@CNCF is denser and flatter than NF. The excellent cycle behavior of NF@CNCF can be attributed to the high lithiophiliciy of CoN, the strong SEI layer caused by CoF_2, and fast Li$^+$ transfer by the nanosheet structure.

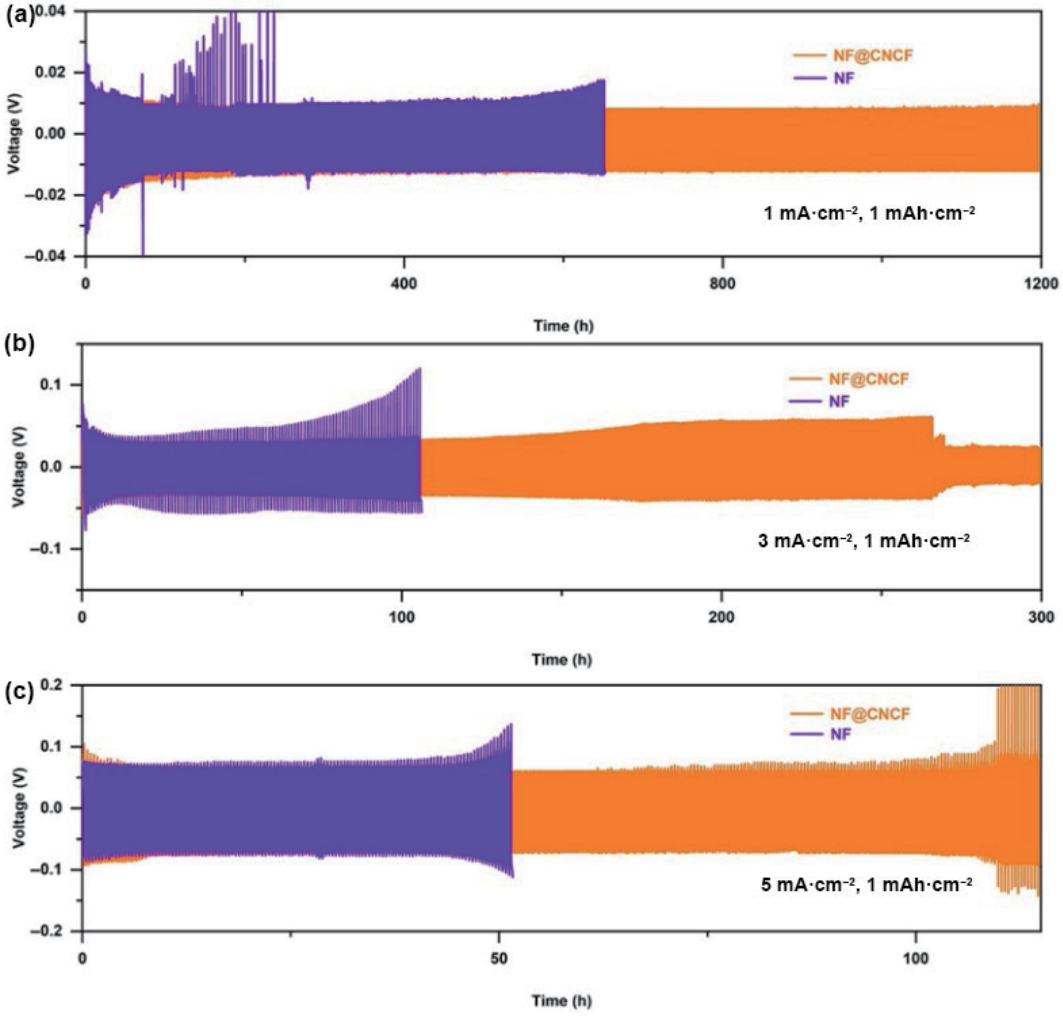

Figure 5 (a)–(c) With the capacity of 1 mAh·cm^{-2}, the cycle performances of the symmetric cells with NF@CNCF and NF with 5 mAh·cm^{-2} deposited Li at 1, 3, and 5 mA·cm^{-2}, respectively.

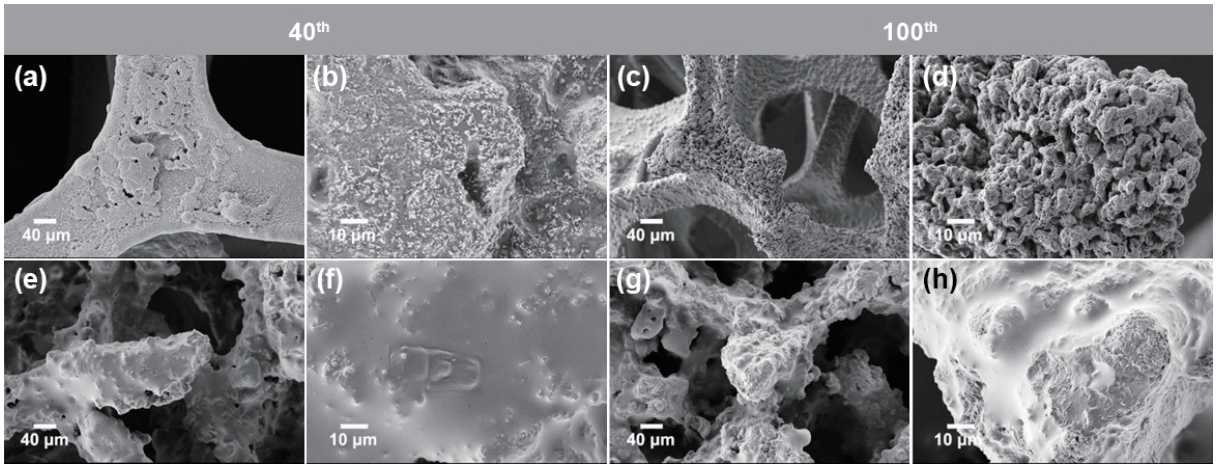

Figure 6 Under 1 mA·cm^{-2} with 1 mAh·cm^{-2}, the SEM images of Li/NF after (a) and (b) 40 and (c) and (d) 100 cycles at different magnifications; the Li/NF@CNCF after (e) and (f) 40 and (g) and (h) 100 cycles.

To measure the capacity retention of CNCF, the NF||Li and NF@CNCF||Li cells were packed and tested at different current densities. The CE of LMAs is defined as the ratio of discharge and charge capacity in the collector [37]. In this work, the capacity of the CE part is fixed at 1 mAh·cm^{-2}. At 1 mA·cm^{-2} (Fig. 7(a)), the CE of the NF can keep at 98% before 150 cycles and fall rapidly. Under the high current density (3 and 5 mA·cm^{-2}) (Figs. 7(b) and7(c)), the CE of NF rapidly decreases (keeps 97% before 120 cycles at 3 mA·cm^{-2}; keeps 96% before 40 cycles at 5 mA·cm^{-2}), which indicates that the high current density would accelerate the production of inactive Li. Satisfactorily, the CE of NF@CNCF can stable more than 98% over 600 cycles at 1 mA·cm^{-2} (Fig. 7(a)). In addition, the NF@CNCF delivers better electrochemical performance (stable 97% over 300 cycles at 3 mA·cm^{-2}; stable 97% about 200 cycles at 5 mA·cm^{-2}) than NF at the same condition (Figs. 7(b) and 7(c)). In the original cycles, the reason for the increasing CE is the first generation of the SEI layer. According to the curve of capacity and voltage (Fig. 7(d)), the max capacity of the NF is clearly lower than the initial cycles (the curve movesleft).The reason of the decline can be attributed to the

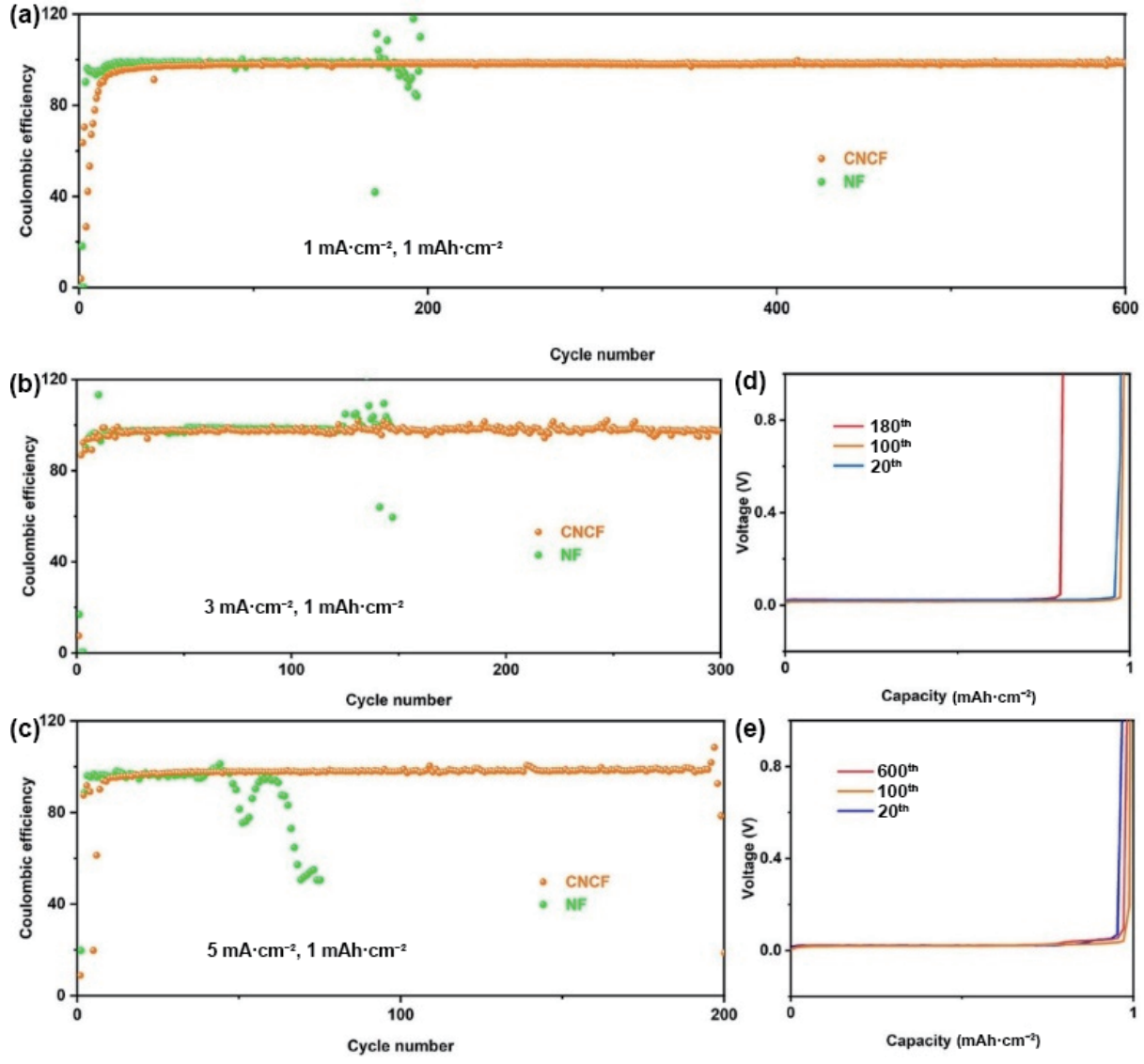

Figure 7 The CE of the NF and CNCF at (a) 1, (b) 3, (c) 5 mA·cm^{-2} with 1 mAh·cm^{-2}; the charge curves of the (d) NF and (e) CNCF at 1 mA·cm^{-2} with 1 mAh·cm^{-2} after different cycles.

rebuilding of SEI layer and the formation of "dead Li". In contrast, the curves of CNCF (Fig. 7(e)) basically coincide after 20, 100, and 600 cycles, which demonstrates that the CNCF has excellent capacity retention. The excellent performance is originated from the attraction to Li metal by the high lithiophilic CNCF.

The EIS is adopted to character the dynamics of the NF@CNCF and NF after different cycles. Figure S11 in the ESM illustrates the EIS profiles of the NF@CNCF and NF after 0, 10, and 20 cycles. With the increase of the cycles (0 to 10), the impedance of NF and NF@CNCF is lower than the original samples. The reason for the decrease in impedance is the formation of stable SEI layer in the process of cycles [38]. Afterward, the impedance of NF after 20 cycles improves due to the unstable solid–liquid interface and generation of "dead Li". On the contrary, the impedance of NF@CNCF still increases from 10 to 20 cycles. So, the SEI layer on CNCF is more stable than NF, which benefits for the charge transfer. As illustrated in Fig. S12 in the ESM, the equivalent circuit was fitted by the ZSimpWin. Herein, the R_s, R_{CNCF}, and R_{NF} (Fig. S12(b) in the ESM) represent the solution resistance, charge transfer resistance in CNCF nanosheets and NF, separately. The CPE_{CNCF}, CPE_{NF}, and Z_w (Fig. S12(a) in the ESM) represent the phase resistance of CNCF and NF, warbulk resistance, orderly. With the calculation (Fig. S11(c) in the ESM), the R_{NF} is 144.08, 95.57, and 109.7 Ω, which is higher than R_{CNCF} (143.04, 83.04, and 52.44 Ω) after 0, 10, and 20 cycles. After 400 cycles (Fig. S11(d) in the ESM), the R_{CNCF} is 13.05 Ω, which means the interface of CNCF and electrolyte is stable. The lower resistance of CNCF plays an important role in fast charge transfer.

As we all know, the SEI layer plays an important role in stable LMAs in the cycles. The content of the SEI layer is complex, which includes Li_2CO_3, Li_2O, and LiF, etc. The existence of LiF can improve the strength and protect the integrity of the SEI layer. To identify the chemical components and valence of the SEI layer after cycles, XPS was preferred to character the NF and NF@CNCF after 20 cycles. Figure S13 in the ESM shows the full XPS spectra of NF and NF@CNCF. Compared with the C detail spectra of simples (Figs. 8(a) and 8(b)), the C–F bond (293.28 eV) significantly appears in the NF@CNCF, which means the F content in the SEI layer of NF@CNCF is more than NF. Figures 8(c) and 8(d) exhibit the F detail spectra of simples, the peaks at 688.79 and 685.21 eV can match with C–F and LiF [39], separately. According to the calculation by Thermo Advantage, the equivalent homogeneous composition of LiF is about 2.91% (NF) and 18.70% (NF@CNCF), respectively. The high content of LiF is from the CoF_2 in the NF@CNCF electrode in the process of cycling, which benefits to construct stable LMAs.

To test the practical application ability of simple, the full cells with NF@CNCF were packed and cycled in the LAND system.

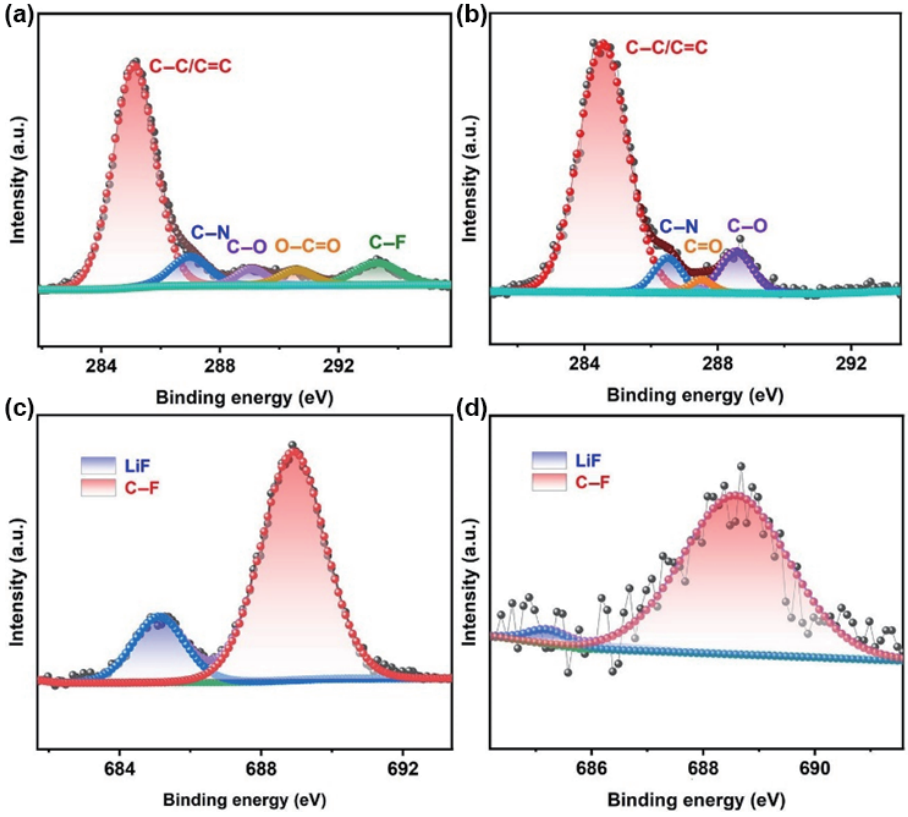

Figure 8 The high-resolution C spectra of (a) NF@CNCF and (b) NF after 40 cycles; the F spectra of (c) NF@CNCF and (d) NF after 40 cycles.

Different from the above cells, the electrodes of the full cells are LFP and Li/NF or Li/NF@CNCF. The specific mass loading of the LFP is 1.66 mg·cm^{-2}. Under 1 C (Fig. 9(a)), the full cells of NF deliver 125.9 mAh·g^{-1} at the first cycle. With the cycling, the specifical capacity slowly decreases to 106.4 mAh·g^{-1} after 130 cycles, and the CE of NF quickly decreases after 125 cycles. Satisfactorily, the full cells of NF@CNCF exhibit higher initial specific capacity (133.88 mAh·g^{-1}) and stability. After 200 cycles, the specific capacity can be kept at 121.2 mAh·g^{-1}, and the CE can maintain above 99%. With the decoration of CNCF, the application potential of LMAs has been significantly improved. In addition, the rate ability of NF@CNCF was tested at 0.5, 1, 2, 3, 5, and 0.5 C (Fig. 9(b)), respectively. As expected, the full cells of NF@CNCF (142.8, 125.4, 107.2, 96.3, 85.9, 71.5, and 140.7 mAh·g^{-1}) exhibit higher specific capacity than NF (132.1, 117.6, 86.7, 69.5, 53.0, 37.8, and 127.4 mAh·g^{-1}) at different current

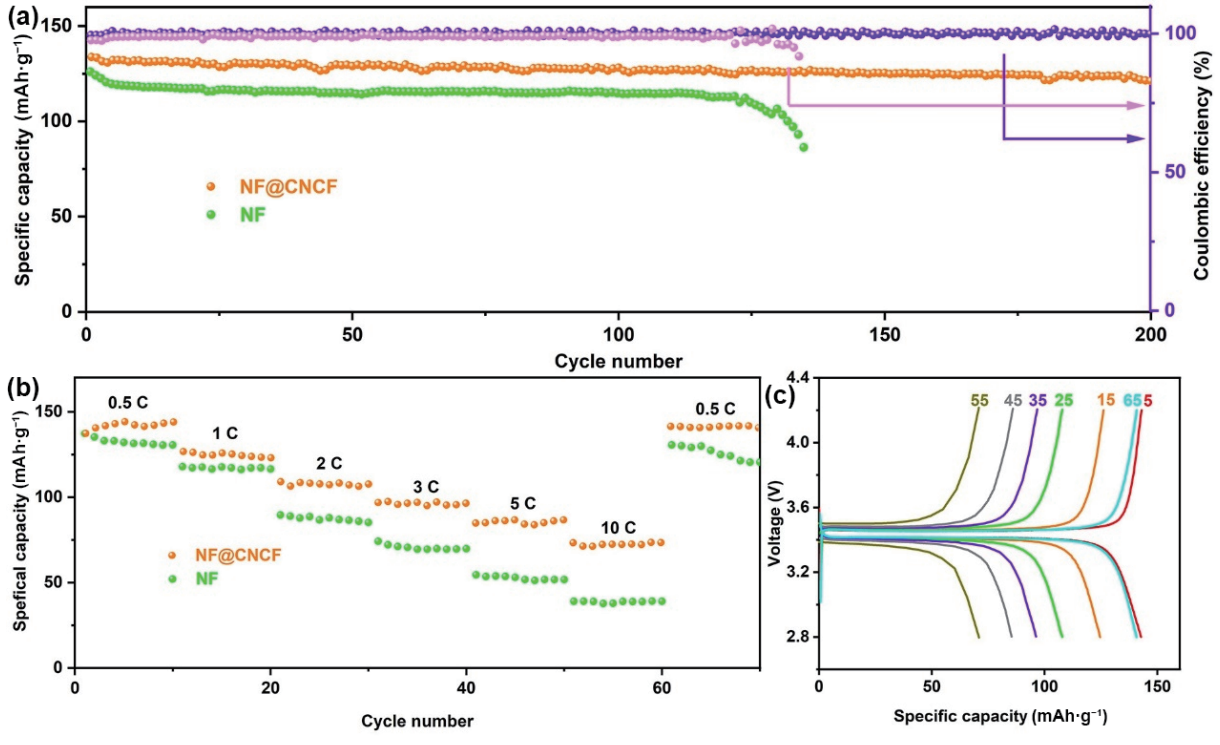

Figure 9 (a) The long cycle performance of Li/NF and Li/NF@CNCF at 1 C. (b) The rate ability of NF and NF@CNCF at 0.5, 1, 2, 3, 5, 10, 0.5 C. (c) The charge–discharge curve of the full cells with Li/NF@CNCF at various currents.

densities. Figure 9(c) is the charge–discharge curve of NF@CNCF at various currents. With the rise of current, the curve moves to the left, which means the decreasing of specific capacity. And, the curve could return to the around of original location when the current decreases to 0.5 C. However, the repeatability of the NF curves is poor (Fig. S14 in the ESM). Besides, the overpotential of the full cells with NF@CNCF (Fig. S15(a) in the ESM) is lower than NF (Fig. S15(b) in the ESM). Therefore, the Li/NF@CNCF possesses pleasing structural stability and electrochemical performance.

4 Conclusions

In summary, a CoN and CoF_2 nanosheet structure was designed and decorated on the Ni foam as the collector for dendrite-free LMAs in this paper. The Ni foam is a classical collector to accommodate the deposited Li for relieving the volume change. The nanosheet structure could uniform the local current distribution, and accelerate the Li^+ transfer as the fast way. Moreover, the high lattice matching of Li and CoN enormously increases the lithiophilicity of Ni foam and reduces the nucleation barrier. Meanwhile, the CoF_2 would add the F content in the interface of electrode and electrolyte, which indicates the increase of LiF phase and the higher strength of the SEI layer. Benefited from the synergies of Ni foam and CoN, CoF_2 nanosheets, the symmetric cells of NF@CNCF reveal superior cycle life and low overvoltage. And, the CE of NF@CNCF remains over 98% after 600 cycles at 1 $mA{\cdot}cm^{-2}$ with 1 $mAh{\cdot}cm^{-2}$. In addition, the full cells of LFP and Li/NF@CNCF deliver satisfactory specific capacity and cycle life. As a result, the NF@CNCF improves the electrochemical performance in LMAs and exhibits potential in the business application.

Acknowledgements

This work was supported by the Fundamental Research Funds for the Central Universities (No. 3132023503). The authors thank Shiyanjia Lab (www.shiyanjia.com) for the XPS test.

Electronic Supplementary Material: Supplementary material (XRD spectra, SEM images, EDS elemental mapping images, XPS spectra, deposition curves, optical images, rate performance, impedance diagram, and charge–discharge curve of full cells) is available in the online version of this article at https://doi.org/10.1007/s12274-023-6298-2.

References

[1] Zhou, T.; Shen, J. D.; Wang, Z. S.; Liu, J.; Hu, R. Z.; Ouyang, L. Z.; Feng, Y. Z.; Liu, H.; Yu, Y.; Zhu, M. Regulating lithium nucleation and deposition via MOF-derived Co@C-modified carbon cloth for stable Li metal anode. *Adv. Funct. Mater.* **2020**, *30*, 1909159.

[2] Zhang, H. Y.; Ju, S. L.; Xia, G. L.; Sun, D. L.; Yu, X. B. Dendrite-free Li-metal anode enabled by dendritic structure. *Adv. Funct. Mater.* **2021**, *31*, 2009712.

[3] Li, S. Q.; Zhang, L.; Liu, T. T.; Zhang, Y. W.; Guo, C. F.; Wang, Y.; Du, F. H. A dendrite-free lithium-metal anode enabled by designed ultrathin MgF_2 nanosheets encapsulated inside nitrogen-doped graphene-like hollow nanospheres. *Adv. Mater.* **2022**, *34*, 2201801.

[4] Liu, B.; Zhang, Y.; Wang, Z. L.; Ai, C. Z.; Liu, S. F.; Liu, P.; Zhong, Y.; Lin, S. W.; Deng, S. J.; Liu, Q. et al. Coupling a sponge metal fibers skeleton with *in situ* surface engineering to achieve advanced electrodes for flexible lithium-sulfur batteries. *Adv. Mater.* **2020**, *32*, 2003657.

[5] Huang, L.; Guan, T. X.; Su, H.; Zhong, Y.; Cao, F.; Zhang, Y. Q.; Xia, X. H.; Wang, X. L.; Bao, N. Z.; Tu, J. P. Synergistic interfacial bonding in reduced graphene oxide fiber cathodes containing Polypyrrole@sulfur Nanospheres for flexible energy storage. *Angew. Chem., Int. Ed.* **2022**, *61*, e202212151.

[6] Salvatierra, R. V.; López-Silva, G. A.; Jalilov, A. S.; Yoon, J.; Wu, G.; Tsai, A. L.; Tour, J. M. Suppressing Li metal dendrites through a solid Li-Ion backup layer. *Adv. Mater.* **2018**, *30*, 1803869.

[7] Huang, L.; Shen, S. H.; Zhong, Y.; Zhang, Y. Q.; Zhang, L. J.; Wang, X. L.; Xia, X. H.; Tong, X. L.; Zhou, J. C.; Tu, J. P. Multifunctional hyphae carbon powering lithium-sulfur batteries. *Adv. Mater.* **2022**, *34*, 2107415.

[8] Jang, J.; Shin, J. S.; Ko, S.; Park, H.; Song, W. J.; Park, C. B.; Kang, J. Self-assembled protective layer by symmetric ionic liquid for long-cycling lithium-metal batteries. *Adv. Energy Mater.* **2022**, *12*, 2103955.

[9] Cui, X. Y.; Cheng, J. C.; Li, C.; Sun, Z. Q.; Li, K. X.; Wang, Y. J.; Fan, X. X.; Tang, S.; Lin, X. D.; Yuan, R. M. et al. A tip-inhibitor interphase embedded with soluble polysulfides for high-voltage Li metal batteries. *Energy Environ. Mater.* **2023**, *6*, e12393.

[10] Jiang, Y.; Jiang, J. L.; Wang, Z. X.; Han, M. R.; Liu, X. Y.; Yi, J.; Zhao, B.; Sun, X. L.; Zhang, J. J. $Li_{4.4}Sn$ encapsulated in hollow graphene spheres for stable Li metal anodes without dendrite formation for long cycle-life of lithium batteries. *Nano Energy* **2020**, *70*, 104504.

[11] Liu, Y.; Qiao, Y.; Zhang, Y.; Yang, Z.; Gao, T. T.; Kirsch, D.; Liu, B. Y.; Song, J. W.; Yang, B.; Hu, L. B. 3D printed separator for the thermal management of high-performance Li metal anodes. *Energy Storage Mater.* **2018**, *12*, 197–203

[12] Cao, W. Z.; Lu, J. Z.; Zhou, K.; Sun, G. C.; Zheng, J. Y.; Geng, Z.; Li, H. Organic–inorganic composite SEI for a stable Li metal anode by *in-situ* polymerization. *Nano Energy* **2022**, *95*, 106983.

[13] Ren, F. H.; Li, Z. D.; Zhu, Y.; Huguet, P.; Deabate, S.; Wang, D. Y.; Peng, Z. Artificial nucleation sites with stable SEI for Li metal anodes by aggressive Al pulverization. *Nano Energy* **2020**, *73*, 104746.

[14] Wang, Q.; Yang, J.; Huang, X. Y.; Zhai, Z. H.; Tang, J. X.; You, J. H.; Shi, C. G.; Li, W. Z.; Dai, P.; Zheng, W. C. et al. Rigid and flexible SEI layer formed over a cross-linked polymer for enhanced ultrathin Li metal anode performance. *Adv. Energy Mater.* **2022**, *12*, 2103972.

[15] Yang, Y. X.; Zhang, C. H.; Zhao, G. F.; An, Q.; Mei, Z. Y.; Sun, Y. J.; Xu, Q. J.; Wang, X. F.; Guo, H. Regulating the electron structure of covalent organic frameworks by strong electron-withdrawing nitro to construct specific Li^+ oriented channel. *Adv. Energy Mater.* **2023**, *13*, 2300725.

[16] Lu, Q. Q.; Jie, Y. L.; Meng, X. Q.; Omar, A.; Mikhailova, D.; Cao, R. G.; Jiao, S. H.; Lu, Y.; Xu, Y. L. Carbon materials for stable Li metal anodes: Challenges, solutions, and outlook. *Carbon Energy* **2021**, *3*, 957–975.

[17] Wang, Q.; Yang, C. K.; Yang, J. J.; Wu, K.; Qi, L. Y.; Tang, H.; Zhang, Z. Y.; Liu, W.; Zhou, H. H. Stable Li metal anode with protected interface for high-performance Li metal batteries. *Energy Storage Mater.* **2018**, *15*, 249–256.

[18] Wang, C. H.; Zhao, Y.; Sun, Q.; Li, X.; Liu, Y. L.; Liang, J. W.; Li, X. N.; Lin, X. T.; Li, R. Y.; Adair, K. R. et al. Stabilizing interface between $Li_{10}SnP_2S_{12}$ and Li metal by molecular layer deposition. *Nano Energy* **2018**, *53*, 168–174.

[19] Yang, Y. X.; Zhang, C. H.; Mei, Z. Y.; Sun, Y. J.; An, Q.; Jing, Q.; Zhao, G. F.; Guo, H. Interfacial engineering of perfluoroalkyl functionalized covalent organic framework achieved ultra-long cycled and dendrite-free lithium anodes. *Nano Res.* **2023**, *16*, 9289–9298.

[20] Su, J.; Pasta, M.; Ning, Z. Y.; Gao, X. W.; Bruce, P. G.; Grovenor, C. R. M. Interfacial modification between argyrodite-type solid-state electrolytes and Li metal anodes using LiPON interlayers. *Energy Environ. Sci.* **2022**, *15*, 3805–3814.

[21] Qiu, F. L.; Ren, S. Y.; Zhang, X. P.; He, P.; Zhou, H. S. A high efficiency electrolyte enables robust inorganic–organic solid electrolyte interfaces for fast Li metal anode. *Sci. Bull.* **2021**, *66*, 897–903.

[22] Liu, D. Q.; Wang, Y. L.; Tong, T.; Luo, G.; Shen, J.; Cai, X. K.

Mesoporous copper-based metal glass as current collector for Li metal anode. *Chem. Eng. J.* **2023**, *451*, 138910.

[23] Liu, Y. H.; Li, Y. F.; Du, Z. Z.; He, C.; Bi, J. X.; Li, S. Y.; Guan, W. Q.; Du, H. F.; Ai, W. Integrated gradient Cu current collector enables bottom-up Li growth for Li metal anodes: Role of interfacial structure. *Adv. Sci.* **2023**, *10*, 2301288.

[24] Xu, R.; Zhou, Y. Y.; Tang, X. X.; Wang, F. Z.; Dong, Q.; Wang, T.; Tong, C.; Li, C. P.; Wei, Z. D. Nanoarray architecture of ultra-lithiophilic metal nitrides for stable lithium metal anodes. *Small* **2023**, *19*, 2205709.

[25] Wang, J. L.; Zhang, Z.; Ying, H. J.; Han, G. R.; Han, W. Q. *In-situ* formation of LiF-rich composite interlayer for dendrite-free all-solid-state lithium batteries. *Chem. Eng. J.* **2021**, *411*, 128534.

[26] Liu, Q.; Wang, R. L.; Liu, Z. F.; Wang, X. S.; Han, G. P.; Liu, H. B.; Li, B. H. A 3D lithiophilic ZIF-8@RGO free-standing scaffold with dendrite-free behavior enabling high-performance Li metal batteries. *J. Mater. Chem. A* **2023**, *11*, 12910–12917.

[27] Liu, S.; Zhang, X. Y.; Li, R. S.; Gao, L. B.; Luo, J. Y. Dendrite-free Li metal anode by lowering deposition interface energy with $Cu_{99}Zn$ alloy coating. *Energy Storage Mater.* **2018**, *14*, 143–148.

[28] Man, J. Z.; Liu, K.; Du, Y. H.; Wang, X. Y.; Li, S.; Wen, Z. S.; Ji, S. J.; Sun, J. C. A stable liquid-solid interface of a lithium metal anode enabled by micro-region meshing. *Nanoscale* **2022**, *14*, 1195–1201.

[29] Tang, D. L.; Yuan, L. X.; Liao, Y. Q.; Jin, W. X.; Chen, J.; Cheng, Z. X.; Li, X.; He, B.; Li, Z.; Huang, Y. H. Improving the cycling stability of lithium metal anodes using Cu_3N-modified Cu foil as a current collector. *Sci. China Mater.* **2022**, *65*, 2385–2392.

[30] Yang, Q. F.; Cui, M. N.; Hu, J. L.; Chu, F. L.; Zheng, Y. J.; Liu, J. J.; Li, C. L. Ultrathin defective C–N coating to enable nanostructured Li plating for Li metal batteries. *ACS Nano* **2020**, *14*, 1866–1878.

[31] Wu, F.; Yuan, Y. X.; Cheng, X. B.; Bai, Y.; Li, Y.; Wu, C.; Zhang, Q. Perspectives for restraining harsh lithium dendrite growth: Towards robust lithium metal anodes. *Energy Storage Mater.* **2018**, *15*, 148–170.

[32] Gong, Y. J.; Heo, J. W.; Lee, H.; Kim, H.; Cho, J.; Pyo, S.; Yun, H. E. J.; Kim, H.; Park, S. Y.; Yoo, J. et al. Nonwoven rGO fiber-aramid separator for high-speed charging and discharging of Li metal anode. *Adv. Energy Mater.* **2020**, *10*, 2001479.

[33] Wang, T. S.; Liu, X. B.; Zhao, X. D.; He, P. G.; Nan, C. W.; Fan, L. Z. Regulating uniform Li plating/stripping via dual-conductive metal-organic frameworks for high-rate lithium metal batteries. *Adv. Funct. Mater.* **2020**, *30*, 2000786.

[34] Jin, X. P.; Huang, G. X.; Zhao, X. M.; Chen, G. L.; Guan, M. J.; Li, Y. S. An *in situ* LiF-enriched solid electrolyte interphase from CoF_2-decorated N-doped carbon for dendrite-free Li metal anodes. *Energy Adv.* **2023**, *2*, 725–732.

[35] Yan, X. L.; Lin, L.; Chen, Q. L.; Xie, Q. S.; Qu, B. H.; Wang, L. S.; Peng, D. L. Multifunctional roles of carbon-based hosts for Li-metal anodes: A review. *Carbon Energy* **2021**, *3*, 303–329.

[36] Zhao, Y. H.; Xu, R.; Zhou, Y. Y.; Wang, F. Z.; Tong, C.; Shao, M. H.; Wang, M.; Li, C. P.; Wei, Z. D. Lattice-matching Ni-based scaffold with a spongy cover for uniform electric field against lithium dendrites. *Chem. Commun.* **2021**, *57*, 9442–9445.

[37] Song, R. F.; Yao, J. M.; Xu, R. N.; Li, Z. X.; Yan, X. L.; Yu, C.; Huang, Z. G.; Zhang, L. Metastable decomposition realizing dendrite-free solid-state Li metal batteries. *Adv. Energy Mater.* **2023**, *13*, 2203631.

[38] Yuan, H. D.; Nai, J. W.; Tian, H.; Ju, Z. J.; Zhang, W. K.; Liu, Y. J.; Tao, X. Y.; Lou, X. W. An ultrastable lithium metal anode enabled by designed metal fluoride spansules. *Sci. Adv.* **2020**, *6*, eaaz3112.

[39] Wang, T. Y.; Zhang, X. L.; Yuan, N.; Sun, C. W. Molecular design of a metal-organic framework material rich in fluorine as an interface layer for high-performance solid-state Li metal batteries. *Chem. Eng. J.* **2023**, *451*, 138819.